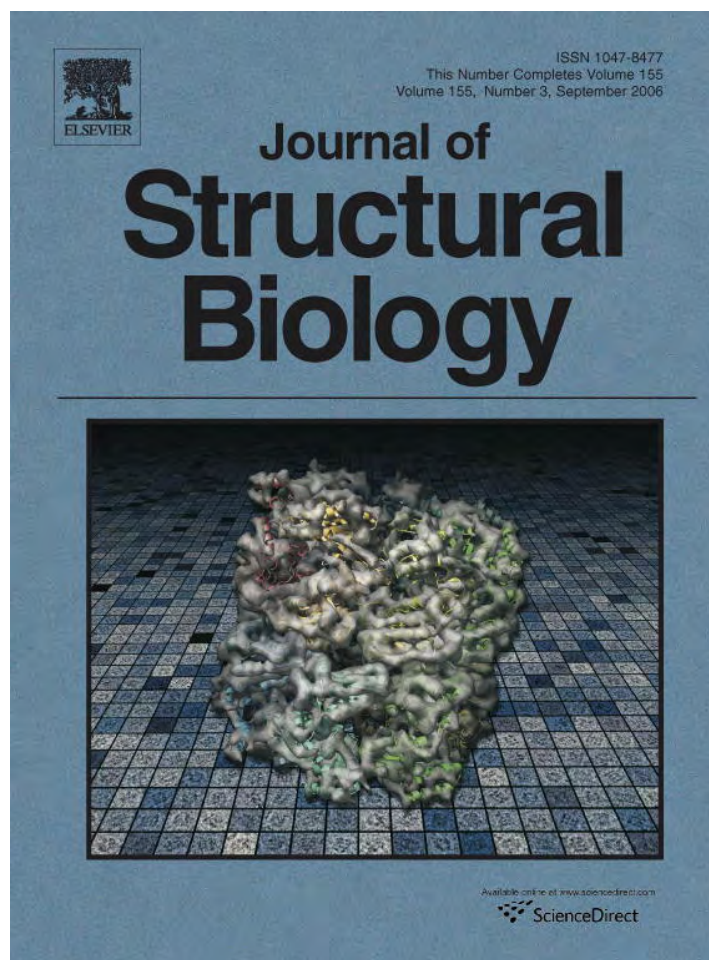


Provided for non-commercial research and educational use only.  
Not for reproduction or distribution or commercial use.



This article was originally published in a journal published by Elsevier, and the attached copy is provided by Elsevier for the author's benefit and for the benefit of the author's institution, for non-commercial research and educational use including without limitation use in instruction at your institution, sending it to specific colleagues that you know, and providing a copy to your institution's administrator.

All other uses, reproduction and distribution, including without limitation commercial reprints, selling or licensing copies or access, or posting on open internet sites, your personal or institution's website or repository, are prohibited. For exceptions, permission may be sought for such use through Elsevier's permissions site at:

<http://www.elsevier.com/locate/permissionusematerial>

# Experimental investigation of the elastic–plastic deformation of mineralized lobster cuticle by digital image correlation

C. Sachs, H. Fabritius, D. Raabe \*

*Max-Planck-Institut für Eisenforschung, Max-Planck-Str. 1, 40237 Düsseldorf, Germany*

Received 8 November 2005; received in revised form 29 May 2006; accepted 10 June 2006

Available online 21 June 2006

## Abstract

This study presents a novel experimental approach to the characterization of the deformation of a mineralized biological composite using arthropod cuticle as a model material. By performing tensile tests combined with a detailed strain analysis via digital image correlation, the elastic–plastic deformation behavior of the endocuticle of the American lobster *Homarus americanus* is examined. The test specimens originate from the pincher and crusher claws. For evaluating the effect of moisture on the deformation behavior, the samples are tested both in dry and in wet state. Sample characterization using the digital image correlation method requires a stochastic spot pattern on the sample surface. Digital images are then taken at subsequent deformation stages during the mechanical test. These images are used to calculate the displacement, the displacement gradient, and the strain fields via pattern correlation. The method is applied both, at a *global* scale to measure with high precision the stress–strain behavior of the bulk cuticle and at a *microscopic* scale to reveal strain heterogeneity, strain patterning, and strain localization phenomena.

© 2006 Elsevier Inc. All rights reserved.

**Keywords:** Biomechanics; Digital image correlation; Mechanical properties; Mineralized cuticle; Strain mapping; Strain patterning

## 1. Introduction

One of the most well known characteristics of Arthropoda is their exoskeleton. This exoskeleton or cuticle consists mainly of chitin and proteins. A characteristic feature of such biological composite materials is their hierarchical organization. The Crustacea represent an important group inside the Arthropoda. Most crustaceans additionally harden their exoskeleton by the incorporation of minerals, mainly calcium carbonate. The cuticle represents a structural unit providing the organism's body with stability, motility through the formation of joints and the attachment of muscles and protection against predators. The American lobster *Homarus americanus* is a large crustacean belonging to the taxon Decapoda. The body of the lobster is divided into three main parts, the head (cephalon), the thorax and the tail (abdomen). The thorax bears

five pairs of legs. The first pair evolved into large claws which differ morphologically in accordance to their function (Fig. 1). The slender one serves as the pincher claw to hold the prey and the bulky one as the crusher claw (Travis, 1963; Vernberg and Vernberg, 1983; Horst and Freeman, 1993).

In the cuticle of *Homarus americanus* three structurally different layers can be distinguished: an outermost epicuticle and an inner procuticle consisting of the exocuticle and the endocuticle (Fig. 2). The epicuticle is a thin waxy layer which provides a permeability barrier to the environment. Both exocuticle and endocuticle are made up of mineralized chitin–protein fibers forming lamellae. The endocuticle makes up around 90 vol% of the cuticle. Local variations in composition and structure of the material provide a wide range of mechanical properties (Hadley, 1986; Vincent, 1990, 2002; Neville, 1993; Vincent and Wegst, 2004; Raabe et al., 2005a,b,c, 2006).

The smallest subunits in the microstructural hierarchy of the lobster cuticle are the chitin molecules (Roer and Dillaman, 1984; Compère, 1995). Their chains are arranged in

\* Corresponding author. Fax: +49 0 731 6792 333.

E-mail addresses: [sachs@mpie.de](mailto:sachs@mpie.de) (C. Sachs), [fabritius@mpie.de](mailto:fabritius@mpie.de) (H. Fabritius), [d.raabe@mpie.de](mailto:d.raabe@mpie.de) (D. Raabe).

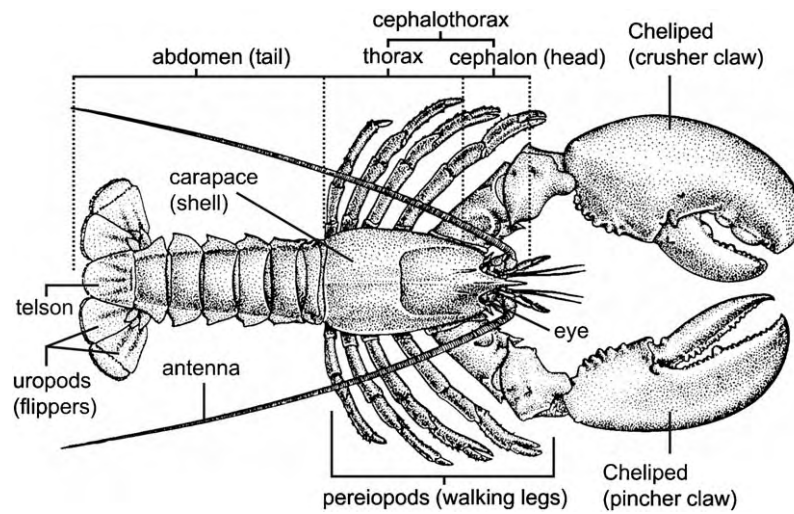


Fig. 1. Schematic drawing of the anatomy of *Homarus americanus* according to Carpenter (2002).

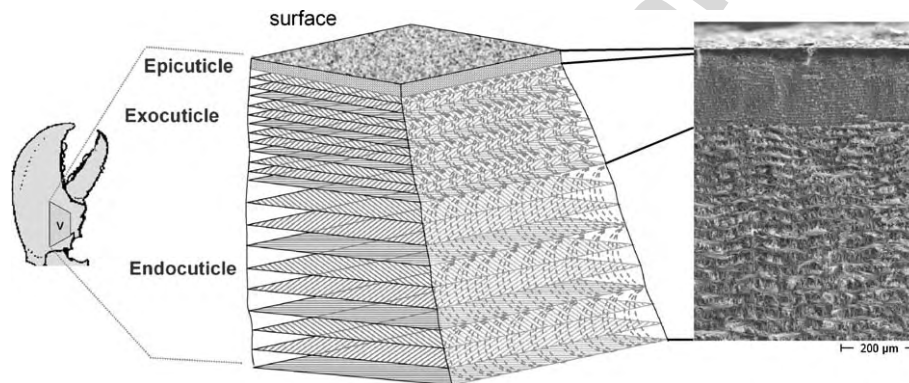


Fig. 2. The organization of the cuticle of *Homarus americanus*, schematic representation and SEM (scanning electron microscope) micrograph of a cross section through the cuticle of a cheliped.

an antiparallel fashion forming  $\alpha$ -chitin, the most abundant of the three crystalline chitin variants occurring in nature (Giraud-Guille, 1990). Eighteen to twenty-five of these chains together form nanofibrils with a diameter of about 2–5 nm and a length of about 300 nm which are wrapped by proteins (Andersen, 1979; Blackwell and Weih, 1980; Andersen, 1999; Shen and Jacobs-Lorena, 1999). These nanofibrils cluster to form long chitin-protein fibers with diameters between 50 and 250 nm which are arranged parallel to each other forming horizontal planes when viewed parallel to the surface of the cuticle. The chitin-protein planes are stacked forming a twisted plywood or Bouligand structure by the rotation of the longitudinal axis of the fibers in super-imposed layers (Giraud-Guille, 1998). A stack that rotates  $180^\circ$  around the normal axis is referred to as one Bouligand or twisted plywood layer (Fig. 3a) (Bouligand, 1970; Giraud-Guille, 1984; Weiner and Addadi, 1997). Characteristic of the lobster cuticle is the presence of a well developed pore canal system with numerous canals penetrating it perpendicular to the surface. The pore canals contain long, soft and probably flexible tubes. The fibers of each chitin-protein plane are

arranged around the lenticellate cavities of the pore canals generating a structure resembling a twisted honeycomb (Fig. 3b) (Raabe et al., 2005a, 2006). In the hard parts of the lobster, the exo- and the endocuticle is mineralized with calcium carbonate in the form of small crystallites located in the spaces between the chitin-protein nanofibrils that serve as a scaffold (Lowenstam, 1981; Mann et al., 1989; Lowenstam and Weiner, 1989; Compère et al., 1992; Giraud-Guille and Bouligand, 1995; Mann, 1995; Manoli et al., 1997; Dillaman et al., 2005). Additionally, the cuticle also contains a considerable amount of amorphous calcium carbonate (Raz et al., 2002; Becker et al., 2005).

The cuticle of *Homarus americanus* is known to have remarkable mechanical properties (Raabe et al., 2005b) which make this material an ideal candidate for the joint investigation of its microscopic structure (Raabe et al., 2006) and the resulting elastic-plastic deformation behavior.

Standardized methods for the investigation of mechanical properties of materials require specific geometry and certain well defined minimum dimensions of the test specimens. Due to its size, thickness and morphology, the cuticle

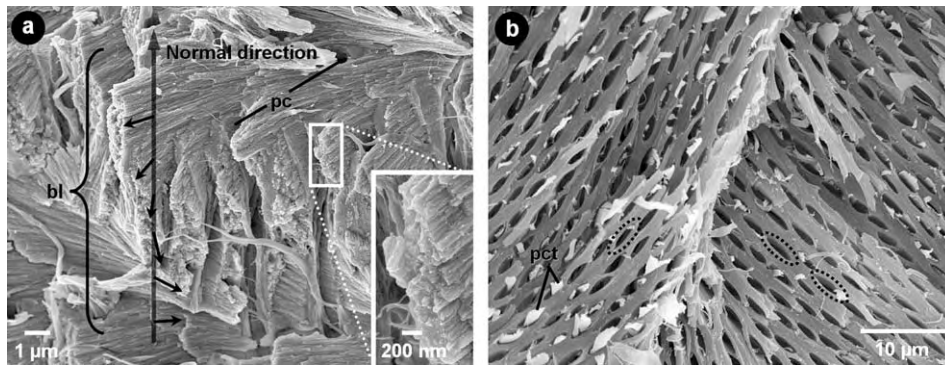


Fig. 3. Microstructure of air-dried endocuticle from the lobster *Homarus americanus* revealed by scanning electron microscopy. (a) Fracture surface of a transversally broken piece of cuticle exposing the broken mineralized chitin-protein fibers and pore canals (pc), some of which are longitudinally fractured. The insert shows a detail image of fractured fibers. They form stacked horizontal planes where the fiber direction (black arrows) rotates around the normal axis of the cuticle (semitransparent arrow). Every stack of planes rotated  $180^\circ$  is referred to as one Bouligand layer (bl). (b) Sample fractured parallel to the surface showing the honeycomb structure formed by the parallel chitin protein fibers which are arranged around the cavities of the pore canal system (encircled areas). The pore canals contain flexible tubes (pct).

of lobsters is very suitable for miniaturized mechanical testing. Owing to the complex hierarchical internal structure of cuticle with its different structural components and probably different micromechanical mechanisms that may occur at different length scales (Gao et al., 2003), such mechanical experiments should fulfill two criteria. First, they should be capable to map *integral* mechanical data at the macroscopic scale and yet, should at the same time be fine enough in dimension to inspect *local* heterogeneity at the microscopic scale. Integral mechanical properties of composite materials are the structural stiffness  $s_{st}$ , the yield strain  $\varepsilon_y$ , the yield stress  $\sigma_y$ , the strain to fracture  $\varepsilon_f$  and the stress to fracture  $\sigma_f$ . These characteristic measures are determined from unidirectional stress–strain curves obtained by monitoring the force taking effect during elongation of the test specimen. One standard method for the measurement of elongation in material testing is the use of extensometers. The engineering strain,  $\varepsilon$ , is defined by the ratio of the elongation of the sample,  $\Delta l$ , to its initial length,  $l_0$ ,  $\varepsilon = \Delta l/l_0$ . The engineering stress,  $\sigma$ , is defined by the ratio of the force,  $F$ , to the initial cross-section,  $A_0$ , of the test specimen,  $\sigma = F/A_0$ . The ratio of stress and strain in the linear elastic part of the stress–strain curve of the material determines its structural stiffness,  $s_{st} = \sigma/\varepsilon$ . In biological materials the structural stiffness  $s_{st}$  describes the mechanical response in the linear elastic part of the stress–strain curve more precisely than the Young's modulus commonly used in mechanical testing of homogeneous materials like metals or polymers (Raabe et al., 2005b). In these homogeneous bulk materials the linear part of the stress–strain curve is equal to the intrinsic elastic modulus and reflects the nature of the chemical bonds inside the material. In heterogeneous and hierarchically structured composite materials the elastic response is the sum of the intrinsic elastic properties of all components and is strongly influenced by its structural attributes. Hence, in arthropod cuticles the elastic response is defined by the elastic properties of components like the chitin fibrils and biominerals as well as their structural

features like twisted plywood structures or honeycomb structures.

As an alternative to the use of extensometers, global strain data can also be obtained by digital image correlation. One simple and robust method consists in using the displacement field for evaluating the change in the spacing between two reference points upon loading. The initial length  $l_0$  of the region of interest and the actual length  $l_i$  after each elongation interval give the global engineering strain  $\varepsilon_g$  according to  $\varepsilon_{g(i)} = (l_i - l_0)/l_0$ , simply referred to as global strain in the following. The index  $i$  represents the deformation stage which is used as a reference state during the mechanical test. In case of a bone-like shaped flat standard tensile test specimen several such reference points can be defined at both ends of the parallel length of the specimen. These positions correspond to the points which serve in a standard test as contact coordinates for the edges of the extensometers. According to the formula above the average global strain can then be calculated for each deformation step. For creating global mechanical tensile curves the strain data are linked to the corresponding stress data. For the evaluation of Poisson's ratio additional reference points can be defined at both edges of the parallel length of the specimen. Similarly to the global strain, the strain in transverse direction  $\varepsilon_{tr}$  can be determined. Poisson's ratio is defined as the ratio of strain in transverse and in tensile direction in the linear elastic part of the stress–strain curve according to  $\nu = -\varepsilon_{tr}/\varepsilon_g$ .

The digital image correlation method (which is sometimes also referred to as photogrammetry or visioplasticity) has been successfully employed for the determination of the heterogeneity of elastic–plastic displacement and strain fields in metallic materials with heterogeneous microstructure (Raabe et al., 2001; Sachtleber et al., 2002; Raabe et al., 2003). The digital image correlation method is based on the recognition of geometrical changes in the gray scale distribution of surface patterns before and after straining. The natural characteristics of an unprepared sample sur-

face or an artificial stochastic color spray applied to a surface may serve as the input pattern. The initial digital image is mapped by a grid of square facets which is defined by the facet size and the step size. The facet size is the dimension of one single square. The step size  $a$  is the distance between the centers of two adjacent facets according to  $a = y_1 - y_0$  or  $a = x_1 - x_0$  (Fig. 4a). To optimize the spatial resolution the step size can be set smaller than the facet size which leads to an overlap of adjacent facets. The facets are characterized by the gray scale distribution and two- or three-dimensional coordinates are assigned to the facet centers (Zaefferer et al., 2003), Fig. 4.

After elastic–plastic straining, the distorted gray scale pattern is again recognized based on the assumption that the gray scale *distribution* around a certain coordinate remains constant during the straining step. From the change in the border coordinates containing the initial gray scale distribution around the facet center the two-respectively three-dimensional displacement gradient tensor field is determined at each facet center. These data serve as input for deriving the surface components of the local displacement gradient tensor and from that the strain tensor. The digital image correlation method works without any additional artificial regular grid on the sample surface. The spatial resolution of the method, therefore, depends only on the optical resolution of the experimental setup and the quality of the applied pattern. Accurate adjustment of the pattern to the facet size is a crucial factor as each facet must contain enough information to obtain an adequate gray scale distribution. The strain resolution is better than 0.1% since the method uses the match of the complete gray scale distribution. This procedure provides a larger precision than the determination of the new border coordinates in the form of discrete pixel steps.

The objective of our study is to obtain a better understanding of the relationship between the structure and the mechanical properties of the cuticle of the lobster *Homarus americanus* (Vincent and Currey, 1980; Ashby and Wegst, 2004; Currey, 1967, 1996; Hepburn et al., 1975;

Melnick et al., 1996; Weiner and Wagner, 1998; Elices, 2000). Therefore, we performed tensile tests in order to investigate the elastic–plastic deformation behavior of our material by means of strain mapping. In addition to the investigation of integral mechanical data, we also study *micromechanical* aspects such as strain heterogeneity, strain patterning and strain localization phenomena. In particular, the latter aspects have not been addressed yet in the field of the mechanics of mineralized arthropod cuticle.

## 2. Materials and methods

### 2.1. Sample preparation

The specimens used for the tensile tests were taken from the chelipeds of a large adult, non-molting American lobster (*Homarus americanus*) bought from a local food supplier. Four pieces from the pincher and four pieces from the crusher claw were dissected and used to prepare two equal sets of samples, one in dry and one in wet condition. Two samples from each claw were air-dried while the others were stored at low temperatures in a humid atmosphere (4 °C, >90% RH) in order to prevent desiccation. Exposure of these samples to ambient conditions during preparation and testing was kept to a minimum. The cuticle pieces were milled to a thickness of about 1 mm in order to get a coplanar geometry and subsequently machined to the final bone-shaped test specimens (Fig. 5). Before the tensile tests the white sample surfaces were decorated with a graphite aerosol spray to create a stochastic black spot pattern for better contrast as required for digital image correlation. During testing the wet samples were exposed to ambient air without applying any moistening. After the tensile tests, all test specimens were air dried and prepared for scanning electron microscopy. The fractured surfaces were sputter-coated with 10 nm gold, mounted on aluminum sample holders and examined in a CamScan 4 scanning electron microscope.

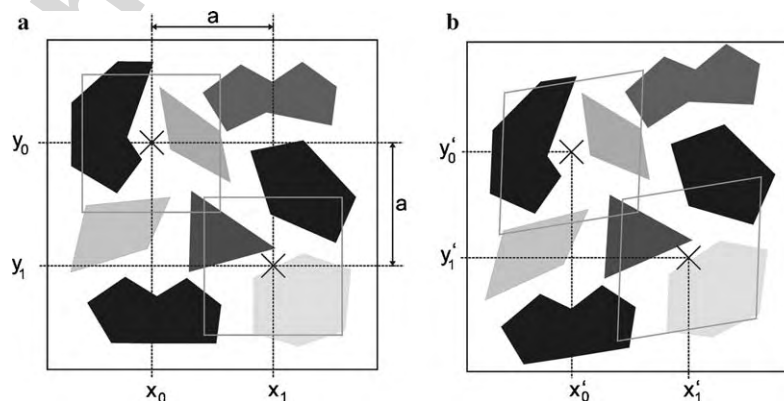


Fig. 4. Pattern recognition of the facets with the center coordinates  $x_0/y_0$  and  $x_1/y_1$  before (a) and after deformation (b) (GOM, 2000). The distance  $a$  is the initial step size which defines the spatial resolution.

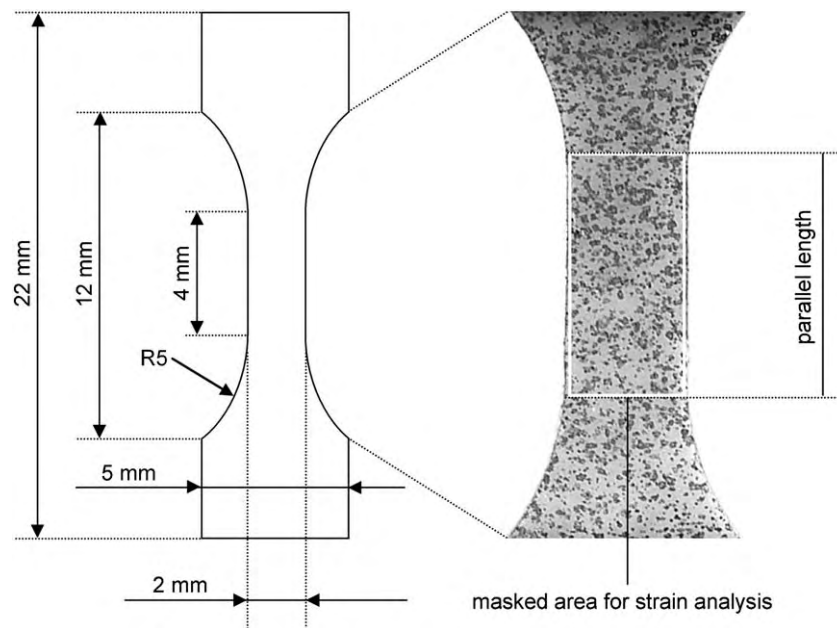


Fig. 5. Schematic drawing of a tensile test specimen including the dimensions and photograph of a spray-coated sample showing the stochastic spot pattern and the area of interest for the strain analysis.

## 2.2. Tensile testing

The tensile tests were performed on a special miniaturized tensile test rack by Kammrath & Weiss GmbH (44141 Dortmund, Germany) constructed for use in scanning electron microscopes. The computerized device features two moveable crossheads allowing the sample to remain in a stable centered position during testing (Fig. 6). The maximum capacity of the load cell amounts to 100 N. The elongation speed amounted to  $2.0 \mu\text{m/s}$  which translates to a strain rate of  $5 \times 10^{-4} \text{ s}^{-1}$ .

In order to record the deformation during the tensile tests, images were taken using two digital cameras, enabling the 3-dimensional localization of each point on the sample surface. The cameras (CCD-1300: VDS Vos-

skühler GmbH, 49084 Osnabrück, Germany) which feature a resolution of up to 1300 dpi were equipped with lenses of 50 mm focal length and a maximum aperture of 2.8 (Schneider-Kreuznach, 55543 Bad Kreuznach, Germany). During testing the aperture was adjusted to its minimum value of 16 to achieve a maximal depth of focus. The camera set-up is controlled by the ARAMIS system (GOM—Gesellschaft für Optische Messtechnik mbH, 38106 Braunschweig, Germany). Digital pictures were taken every 1 s which corresponds to an elongation of  $2 \mu\text{m}$ . The cameras were mounted on a support positioning them perpendicular to the tensile test rack.

## 2.3. Digital image correlation and determination of characteristic data

The series of digital images were processed using the ARAMIS software version V5.4.1–4 (GOM—Gesellschaft für Optische Messtechnik mbH). A rectangular region of interest ( $2 \text{ mm} \times 4 \text{ mm}$ ) was defined on each initial image of the samples which is equivalent to the parallel length (Fig. 5). The facet size was defined to a value of 23 pixels corresponding to  $219 \mu\text{m}$  and the step size was defined to a value of 10 pixels which is equal to a spatial resolution of  $95 \mu\text{m}$ .

The global (engineering) strain data represent the averaged global strain values derived from the displacement of three pairs of reference points which were defined at both ends of the parallel length of the test specimens. Using a sampling rate of 1 image per second and an elongation speed of  $2 \mu\text{m/s}$ , data points were recorded in global strain intervals of 0.05% and linked to the corresponding stress values. For the determination of Poisson's ratio three

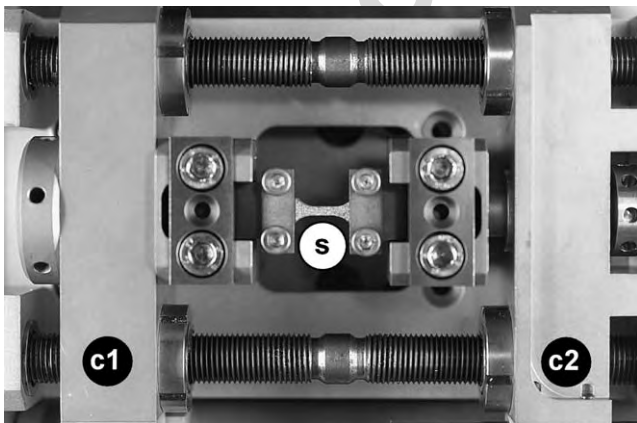


Fig. 6. Miniaturized tensile test rack with two moveable crossheads (c1 and c2). The tensile specimen (s) which is mounted in the center has a length of 12 mm.

additional reference points were defined at both edges of the parallel length of the specimens. Poisson's ratio  $\nu$  was calculated for the linear elastic range of the stress–strain curves which was assessed from 0.1% to 0.5% global strain. For the evaluation of the structural stiffness the same interval was selected to fit the stress–strain curves linearly. The yield strain  $\varepsilon_y$  and the yield stress  $\sigma_y$  were derived from the incept point of the stress–strain curve with a straight line which is shifted 0.01% parallel to the linear part of the curve.

In order to obtain strain maps for each sample, the displacement gradient tensor and the resulting strain tensor were computed at each deformation stage. The final strain map which was derived as an approximation of the strain tensor was then displayed in terms of the von Mises strain. The von Mises strain is given by

$$\varepsilon_M = \sqrt{\frac{2}{3}(\varepsilon_{xx}^2 + \varepsilon_{yy}^2 + \varepsilon_{zz}^2) + \frac{1}{2}(\gamma_{xy}^2 + \gamma_{yz}^2 + \gamma_{zx}^2)}$$

where  $\varepsilon_{xx}$ ,  $\varepsilon_{yy}$  and  $\varepsilon_{zz}$  indicate the normal strain components and  $\gamma_{xy}$ ,  $\gamma_{yz}$  and  $\gamma_{zx}$  indicate shear strain components. Due to the two dimensional (surface) strain analysis conducted on the sample surface, the strain tensor components  $\varepsilon_{zz}$ ,  $\gamma_{yz}$ , and  $\gamma_{zx}$  are unknown. This strain measure is a useful approximation of a deformation state which reduces a strain tensor to an equivalent scalar strain measure.

### 3. Results

#### 3.1. Global stress–strain-behavior

Due to the special geometry required for the test specimens the epi- and the exocuticle were removed during the machining process. The global stress–strain behavior of the material reflects, therefore, only the mechanical properties of the endocuticle. Effects caused by the presence of the other layers are thereby eliminated. The stress–strain curves for the pincher and crusher claws both in the dry and in the wet state are depicted in Fig. 7.

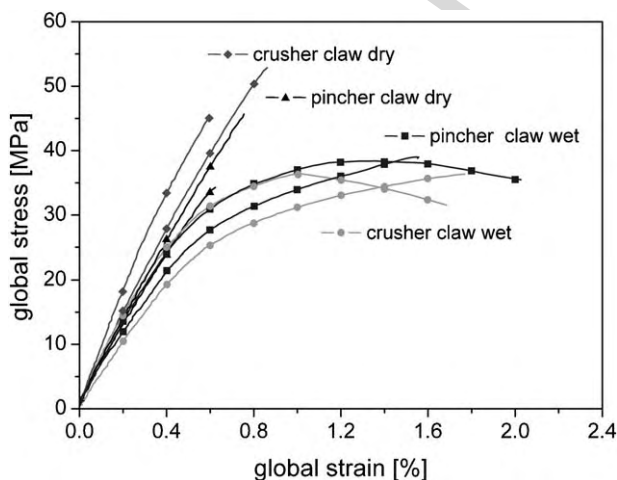


Fig. 7. Global stress–strain behavior of the endocuticle from the pincher and crusher claws both in dry and wet state under tensile loading. For each sample state the curves of two specimens are shown.

The dry samples display a linear stress–strain response. The pincher claw samples reached an average fracture stress of 40.1 MPa at an average strain to fracture of 0.7%. The crusher claw samples failed at an average fracture stress of 48.8 MPa and 0.7% global strain. The wet samples show an extended non-linear range of elastic–plastic deformation before fracture. The linear strain regime for the wet specimens is less than 0.5% global strain. The average fracture stress of the wet pincher claw samples amounts to 37.2 MPa at an average maximum strain of 1.8%. The wet crusher claw samples fail at an average of 34.1 MPa at an average maximum global strain of 1.7%.

Table 1 summarizes the corresponding characteristic mechanical data from the tensile tests, namely, the structural stiffness  $s_{st}$ , the yield strain  $\varepsilon_y$ , the yield stress  $\sigma_y$ , the strain at fracture  $\varepsilon_f$  and the stress at fracture  $\sigma_f$ . The average values of the structural stiffness are 5.8 GPa for the dry pincher claw, 7.0 GPa for the dry crusher claw, 4.9 GPa for the wet pincher claw, and 4.8 GPa for the wet crusher claw. The average values of Poisson's ratio are 0.43 for the dry pincher claw, 0.34 for the dry crusher claw, 0.33 for the wet pincher claw, and 0.34 for the wet crusher claw. The yield strain and yield stress are not defined for the dry pincher claw and dry crusher claw. The average yield strain for the wet samples was about 0.5%. The corresponding average yield stress which marks the onset of plastic flow, was 26.6 MPa for the wet pincher claw and 25.8 MPa for the wet crusher claw.

#### 3.2. Fracture surfaces

The appearance of the fracture surface of one sample from each claw both in dry and in wet condition was investigated using scanning electron microscopy (Figs. 8 and 9).

##### 3.2.1. Pincher claw—dry

The overview of the fractured dry pincher claw shows a relatively smooth surface with very few and flat disruptions. Narrow grooves remaining from cleaved cuticular pores oriented in normal direction recur on the fracture surface approximately every 100–200  $\mu\text{m}$ . The horizontal pattern of the twisted plywood layers appears distinct and even (Fig. 8a). At higher magnifications, details of the endocuticle microstructure become visible. The fractured stacked twisted plywood layers reveal two main fracture patterns. In areas where the stacked fibers are oriented parallel to the fracture surface and in the adjacent areas above and below where the fiber orientation rotates up to about 30° in relation to the fracture surface, the structure is separated mainly along the long axis of the fibers forming short overlapping platelets. Between these areas the fibers forming the stacked planes are oriented perpendicular and rotated up to 70° in both directions to the fracture surface. These stacks of fibers are broken exposing cross- or rather oblique sections. On the whole fracture surface the exposed cavities of longitudinally cleaved pore canals become visible. Occasionally flexible tubes which are

Table 1  
Mechanical properties derived from the global stress–strain curves

Sample	$s_{st}$ (GPa)	$\nu$	$\epsilon_y$ (%)	$\sigma_y$ (MPa)	$\epsilon_f$ (%)	$\sigma_f$ (MPa)
Pincher claw dry	$5.8 \pm 0.4$	$0.43 \pm 0.00$	—	—	$0.7 \pm 0.09$	$40.1 \pm 7.9$
Crusher claw dry	$7.0 \pm 0.8$	$0.34 \pm 0.01$	—	—	$0.7 \pm 0.19$	$48.8 \pm 5.8$
Pincher claw wet	$4.9 \pm 0.6$	$0.33 \pm 0.03$	$0.5 \pm 0.04$	$26.6 \pm 3.2$	$1.8 \pm 0.33$	$37.2 \pm 2.5$
Crusher claw wet	$4.8 \pm 0.6$	$0.34 \pm 0.06$	$0.5 \pm 0.05$	$25.8 \pm 5.9$	$1.7 \pm 0.06$	$34.1 \pm 3.6$

The properties determined are the average values of the samples from each location and testing condition including their standard deviation: structural stiffness  $s_{st}$ , Poisson's ratio  $\nu$ , yield strain  $\epsilon_y$ , yield stress  $\sigma_y$ , strain to fracture  $\epsilon_f$  and stress to fracture  $\sigma_f$ .

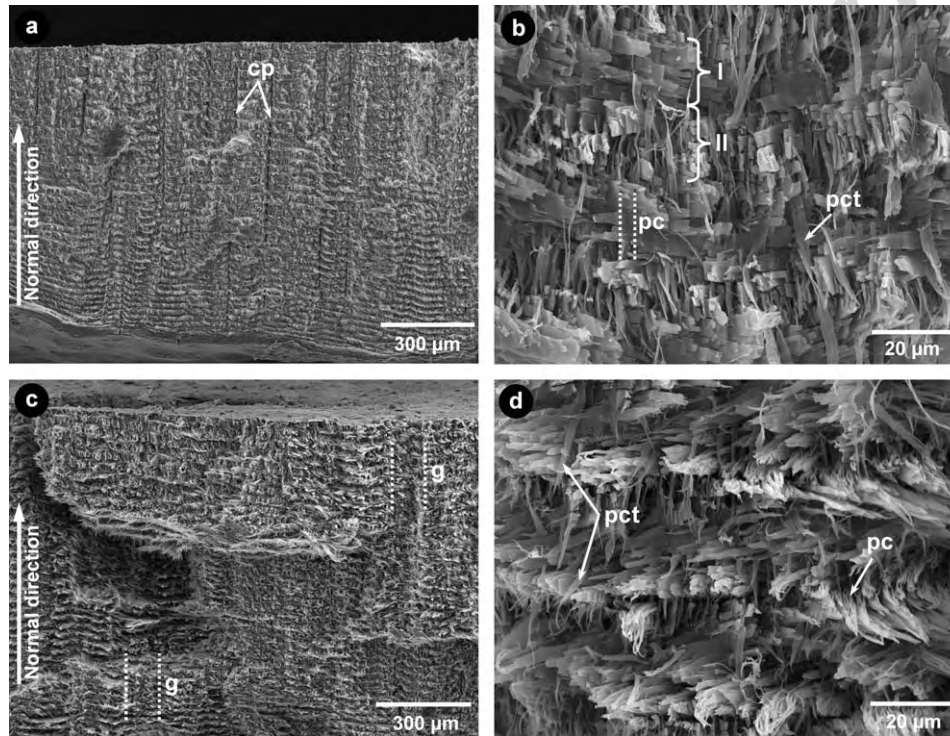


Fig. 8. Fracture surfaces of the pincher claw in the dry (a and b) and in the wet (c and d) state. (a) Overview of the dry pincher claw showing the smooth surface with numerous cleaved cuticular pores (cp). (b) Detail image displaying the fracture modes of fibers oriented more parallel (I) and fibers oriented closer to perpendicular (II) to the fracture surface. (c) Overview of the wet pincher claw showing the corrugated surface with numerous deep irregular grooves (g, indicated by dashed lines). (d) Detail image showing the distorted twisted plywood structure with drawn-out pore canals (pc) and irregularly protruding pore canal tubes (pct).

detached from the pore canals protrude out of the fractured structure. In some areas where the fiber stacks are fractured obliquely to the global fracture plane, the honeycomb structure of the twisted plywood layers can be observed (Fig. 8b).

### 3.2.2. Pincher claw—wet

The overview of the fractured wet pincher claw shows a corrugated surface with coarse and deep disruptions. This appearance is caused by numerous irregular grooves which are oriented in normal direction and about 100–200  $\mu\text{m}$  wide. Cuticular pores such as are seen in the dry samples are not distinguishable. The fracture surface shows a free-standing wedge originating from crack separation during fracture (Fig. 8c). The detail image shows numerous broken fiber bundles and flexible tubes belonging to the pore canal system standing out from the fracture surface in irregular angles. The stacked twisted plywood layers can

still be distinguished, but structural differences between areas where the fiber orientation is more parallel and areas where the fiber orientation is closer to perpendicular to the fracture surface are not very distinct. Portions of the original honeycomb structure can be observed occasionally protruding out of both areas, but the pore canals between the fiber planes are drawn-out and look distorted (Fig. 8d).

### 3.2.3. Crusher claw—dry

The dry crusher claw has a plain and relatively smooth fracture surface with cleaved cuticular pores oriented in normal direction recurring every 100–200  $\mu\text{m}$ . The pattern of the twisted plywood layers is generally distinct and even and is vague only in some small areas (Fig. 9a). At high magnifications the original twisted plywood structure appears quite well preserved. The stacks of fibers forming short overlapping platelets which are oriented more parallel to the fracture surface and the exposed cross sections of

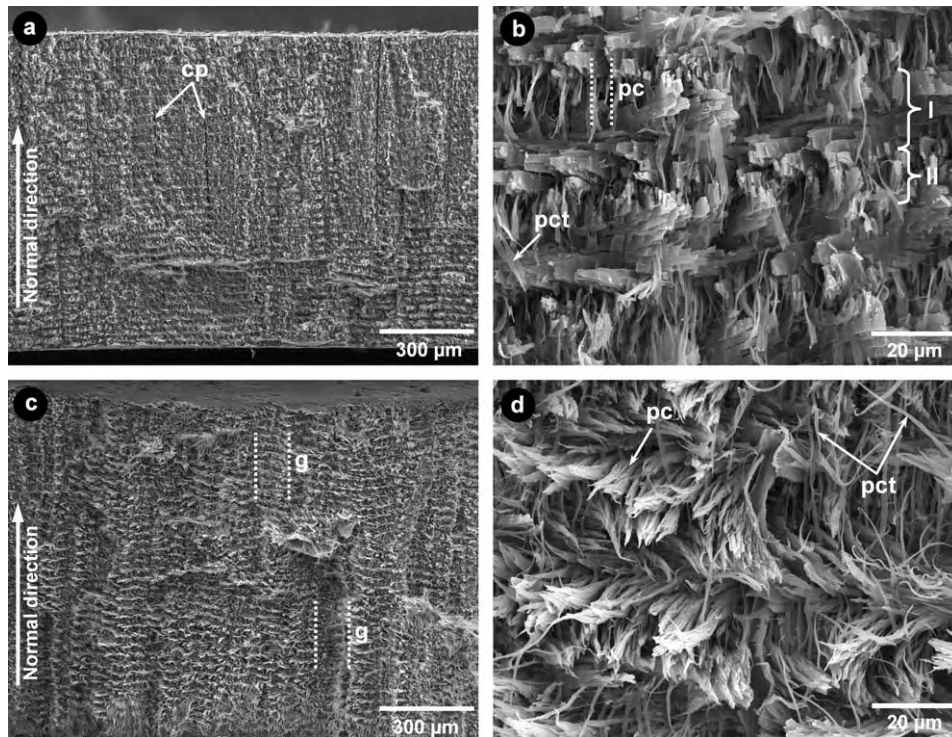


Fig. 9. Fracture surface of the crusher claw in the dry (a and b) and in the wet (c and d) state. (a) Overview of the dry crusher claw showing the smooth surface and numerous cleaved cuticular pores (cp). (b) Detail image displaying the fracture modes of fibers oriented more parallel (I) and fibers oriented closer to perpendicular (II) to the fracture surface. (c) The corrugated and uneven surface of the wet crusher claw with numerous deep irregular grooves (g, indicated by dashed lines). (d) Detail image showing the distorted twisted plywood structure with drawn-out pore canals (pc) and irregularly protruding pore canal tubes (pct).

the stacked fiber planes oriented closer to perpendicular to the fracture surface are equally well defined as in the dry pincher claw. In the obliquely fractured twisted plywood layers its inner honeycomb structure is clearly visible. A small number of the flexible pore canal tubes protrude from the fracture surface (Fig. 9b).

#### 3.2.4. Crusher claw—wet

The overview of the wet crusher claw shows an uneven and corrugated surface with numerous deep grooves about 100–200  $\mu\text{m}$  wide and oriented in normal direction to the endocuticle surface. In contrast to the dry sample, cuticular pores can not be distinguished (Fig. 9c). In the detail image the rotating stacks of fiber planes of the twisted plywood structure can still be distinguished, but the broken fiber bundles stand out from the fracture surface in very irregular angles. Numerous torn and distorted flexible tubes of the pore canal system are distributed between the broken fiber bundles. The original honeycomb structure of the twisted plywood layers can only be guessed in some of the larger pieces of fiber bundles protruding from the surface (Fig. 9d).

### 3.3. Strain analysis

#### 3.3.1. Strain maps

In order to investigate the strain evolution not only at a global but also at a local microscale, strain mappings of a previously defined surface area (Fig. 5) of all samples were

created (Figs. 10–13). For each sample, four strain maps with increasing global (engineering) strain  $\varepsilon_g$  are displayed. For the dry samples the selected strain levels are 0.2%, 0.4%, 0.6% and the strain value just before fracture and for the wet samples 0.4%, 0.8%, 1.2% and the strain value just before fracture. The mapped local strain is displayed in terms of von Mises strain  $\varepsilon_M$ . For the dry samples the scale range was defined from 0% to 1.5% and for the wet samples from 0% to 5.0%.

The samples of the dry pincher claw show a heterogeneous strain pattern with relatively evenly distributed alternating band shaped domains of very low and slightly elevated strain at the beginning of the tensile test ( $\varepsilon_g$  0.2%) (Fig. 10a and b). These domains are oriented perpendicular to the tensile axis and their overall pattern is preserved with increasing global strain ( $\varepsilon_g$  0.4% and 0.6%) while the local strain is gradually elevated. Before fracture, small but strong strain localizations appear on the margins of the monitored sample area which expand abruptly. The final failure of the samples does not occur necessarily at the strongest recorded strain localizations. In the case of specimen 1 the failure is initialized at a small spot of high strain (dashed line in Fig. 10a,  $\varepsilon_g$  0.62%) whereas in specimen 2 none of the visible strain localizations are involved in the final cracking (dashed lines in Fig. 10b,  $\varepsilon_g$  0.8%).

The strain maps obtained for the dry crusher claw (Fig. 10c and d) reveal a heterogeneous strain pattern which is also characterized by alternating band shaped

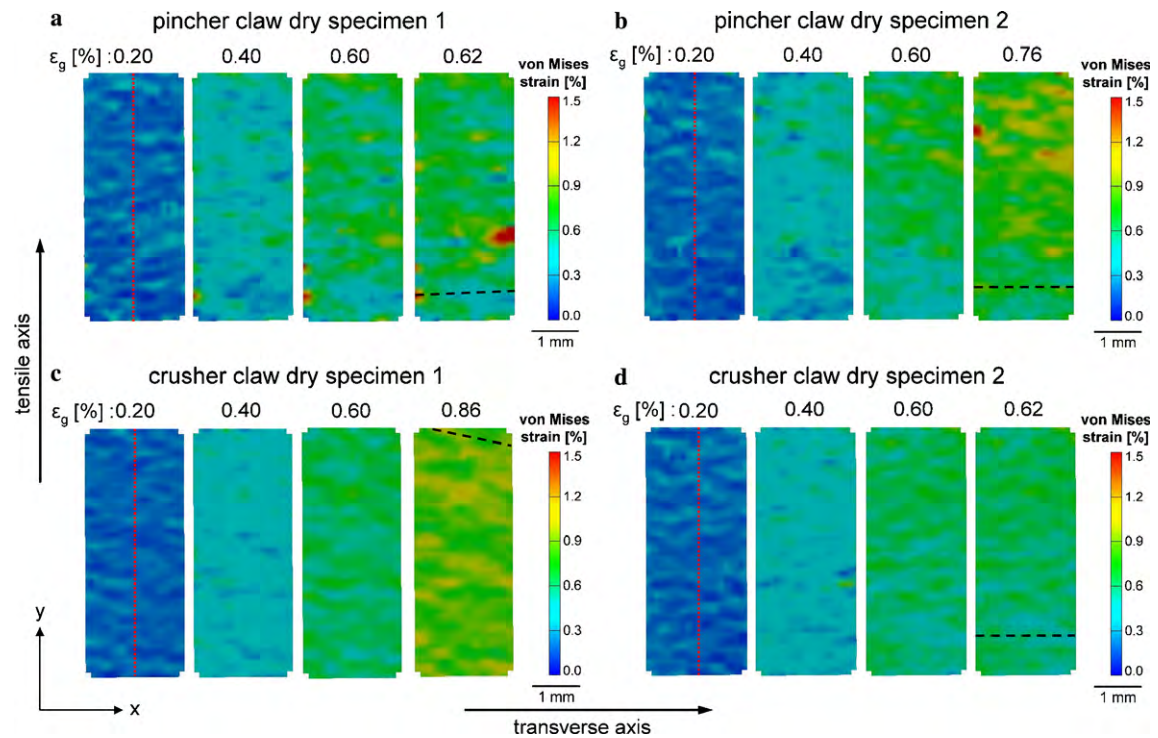


Fig. 10. Strain analysis of endocuticle from the dry pincher and crusher claw. Strain maps showing the strain evolution of the local von Mises strain  $\epsilon_M$  in the parallel length at four subsequent levels of global (engineering) strain  $\epsilon_g$ . The strain map with the highest level of global strain for each sample shows the local strain distribution immediately before the final failure. The red dotted line in the center of the strain maps marks the section for the strain profile. The pathway of the crack is indicated by the black dashed line.

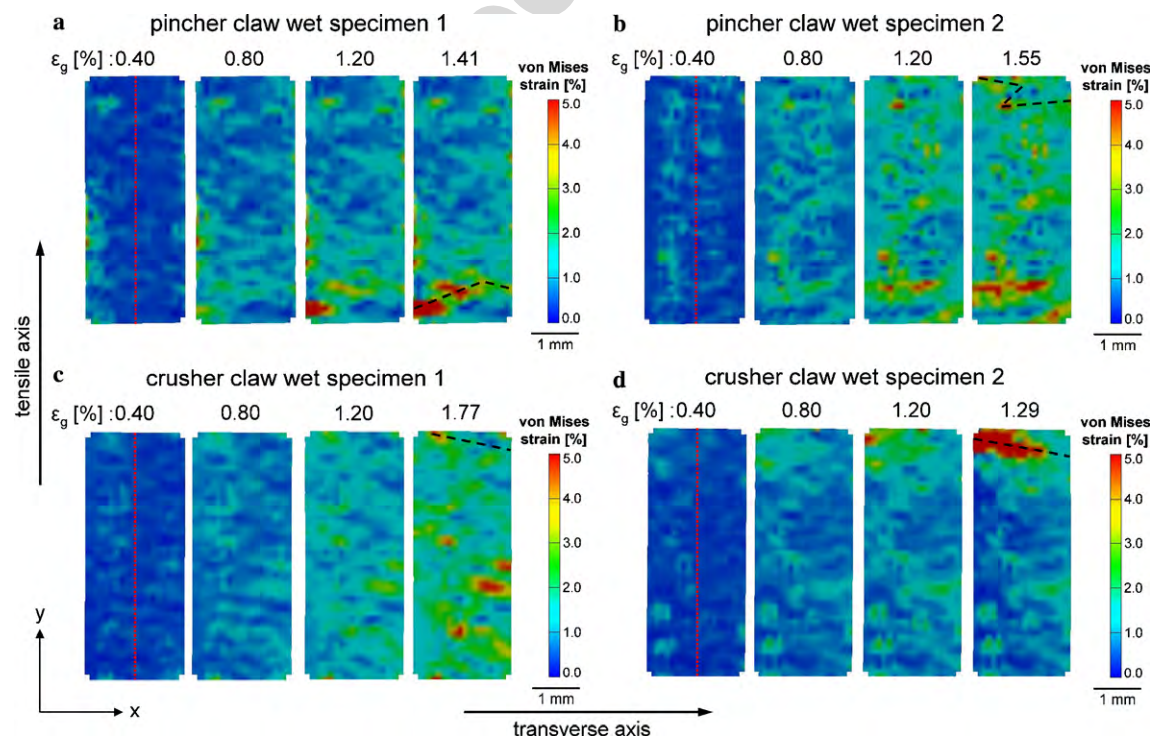


Fig. 11. Strain analysis of endocuticle from the wet pincher and crusher claw. Strain maps showing the strain evolution of the local von Mises strain  $\epsilon_M$  in the parallel length at four subsequent levels of global (engineering) strain  $\epsilon_g$ . The strain map with the highest level of global strain for each sample shows the local strain distribution immediately before the final failure. The red dotted line in the center of the strain maps marks the section for the strain profile. The pathway of the crack is indicated by the black dashed line.

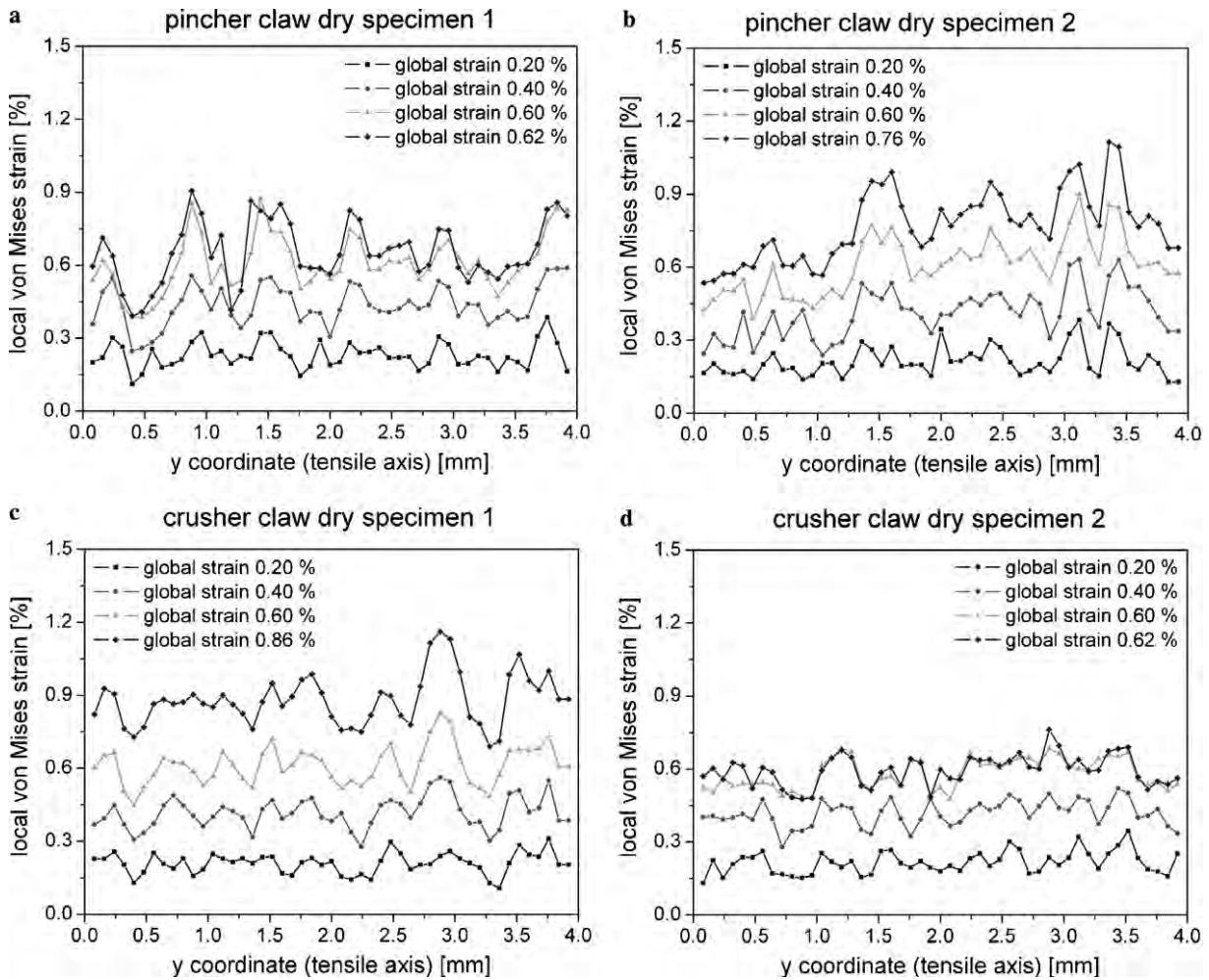


Fig. 12. Strain analysis of endocuticle from the dry pincher and crusher claw. The evolution of the strain profile in the center of the strain maps along the tensile axis is shown. Each curve displays the development of the local von Mises strain  $\epsilon_M$  of the corresponding strain map at a distinct global (engineering) strain  $\epsilon_g$ .

domains of very low and slightly higher local strain ( $\epsilon_g$  0.2% and 0.4%) which is preserved with increasing global strain ( $\epsilon_g$  0.6%) and resembles the pattern seen in the dry pincher claw. The variation in lower and higher local strain in the patterns at a given global strain appears less pronounced than in the samples of the dry pincher claw. Strong spots of localized strain can not be observed before fracture, making it impossible to predict the areas where the final fractures occur (dashed lines in Fig. 10c,  $\epsilon_g$  0.9% and 10d,  $\epsilon_g$  0.62%).

The local strain analysis of wet pincher claw samples (Fig. 11a and b) shows a heterogeneous strain pattern at the beginning ( $\epsilon_g$  0.4%) with large areas of very low strain interspersed with spots of high local strain. During the following stages, these spots expand forming large domains of increased strain while in some areas the local strain remains static ( $\epsilon_g$  0.8% and 1.2%). Many of the initial spots of higher strain develop into small localizations of very high strains. In specimen 1 the final failure occurs at the site of such a strain localization (dashed line in Fig. 11a,  $\epsilon_g$  1.4%). In specimen two the final fracture goes through a

strain localization but is initiated outside of the parallel length at the radius of the test specimen (dashed line in Fig. 11b,  $\epsilon_g$  1.6%).

The endocuticle of the wet crusher claw (Fig. 11c and d) shows a heterogeneous strain pattern ( $\epsilon_g$  0.4%) similar to that of the wet pincher claw but with slightly lower values for the areas with high local strain. The small areas of elevated local strain expand and form larger domains of high local strain during the course of the test ( $\epsilon_g$  0.8% and 1.2%). In some of these domains spots with very high local strain develop in the last stage before fracture. Both samples fail close to the radius of the tensile test specimens and the final fracture goes through a small spot of very high localized strain in specimen 1 (dashed line in Fig. 11c,  $\epsilon_g$  1.8%) and through a larger area of very high localized strain in specimen 2 (dashed line in Fig. 11d,  $\epsilon_g$  1.3%).

### 3.3.2. Strain profiles

For a more detailed local strain analysis, a section was defined along the longitudinal tensile axis in the center of each sample (Figs. 10 and 11). The four curves in every

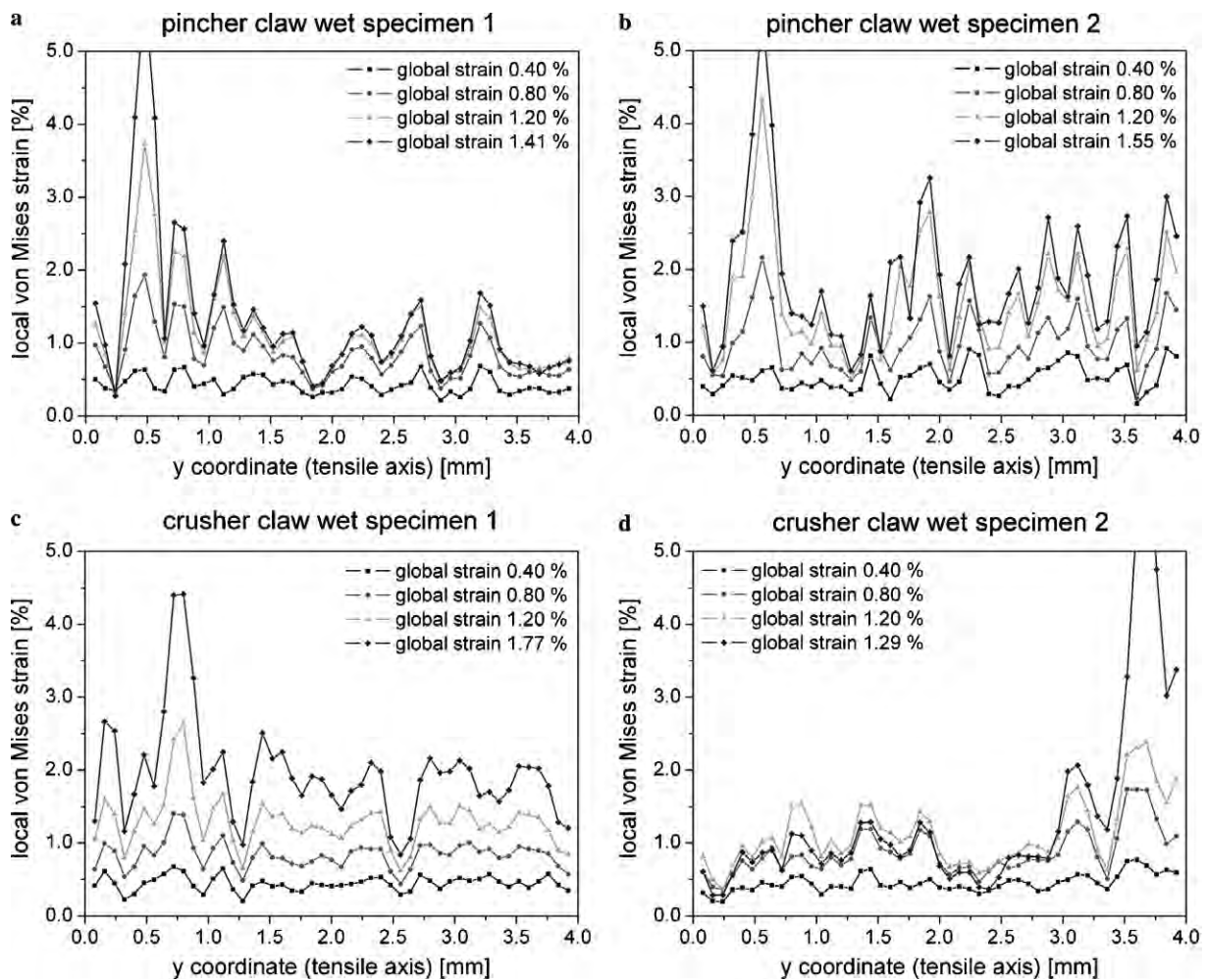


Fig. 13. Strain analysis of endocuticle from the wet pincher and crusher claw. The evolution of the strain profile in the center of the strain maps along the tensile axis is shown. Each curve displays the development of the local von Mises strain  $\epsilon_M$  of the corresponding strain map at a distinct global (engineering) strain  $\epsilon_g$ .

diagram display the evolution of the von Mises strain profiles at each level of global (engineering) strain  $\epsilon_g$  for each sample. The strain profiles show the distribution of the von Mises strain  $\epsilon_M$  along the tensile axis in the center of the tensile test specimen with respect to the initial length of the sample. The average spacing between neighboring maximum or minimum strain levels defines the wavelength of the strain patterning. The difference between the upper and lower threshold given by the averaged maximum and minimum values of the local strain profile defines the profile amplitude. The wavelength and the profile amplitude were determined at the global (engineering) strain level where the local strain profile becomes most concise, namely at 0.6% for the dry samples and 1.2% for the wet samples (see Table 2).

The local strain analysis of the dry pincher claw shows periodically distributed strain maxima for all stages of the tensile test. The average wavelength of the strain profile is 404  $\mu\text{m}$  and the profile amplitude amounts to about 0.24% von Mises strain. The profiles for the different global strain levels look similar and are merely shifted to higher

von Mises strain values with increasing global strain (Fig. 12a and b).

The local strain profiles of the dry crusher claw samples show periodically distributed strain maxima similar to those of the dry pincher claw samples. The average wavelength of the strain profile is 458  $\mu\text{m}$  and the corresponding profile amplitude is about 0.18% von Mises strain. The profiles at different global strain levels look similar but are also shifted to higher von Mises strain values with increasing global strain (Fig. 12c and d).

The local strain analysis of the wet pincher claw (Fig. 13a and b) shows a relatively flat curve with comparatively indistinct peaks for low global strain ( $\epsilon_g$  0.4%). With increasing global strain ( $\epsilon_g$  0.8% and 1.2%) the local von Mises strain reaches very high values in the peaks while the strain values in the valleys increase much slower. The average wavelength of the strain profile is in the order of 470  $\mu\text{m}$  with an average profile amplitude of about 1.06%.

The strain profiles of the wet crusher claw (Fig. 13c and d) show an evolution of the local von Mises strain similar to the samples of the wet pincher claw with a shallow curve

Table 2  
Variables derived from the sections along the center of the strain maps

Sample	Wavelength of strain profiles ( $\mu\text{m}$ )	Lower threshold (%)	Upper threshold (%)	Profile amplitude (%)	Global strain (%)
Pincher claw dry	404	0.54	0.78	0.24	0.6
Crusher claw dry	458	0.52	0.70	0.18	0.6
Pincher claw wet	470	0.83	1.89	1.06	1.2
Crusher claw wet	444	0.86	1.61	0.75	1.2

The properties determined include the average wavelength of the profile, the average lower threshold and the average upper threshold as well as the average profile amplitude (von Mises strain). The variables are evaluated for a global strain of 0.6% in the dry samples and of 1.2% in the wet samples.

at low global strain ( $\varepsilon_g$  0.4%) and an irregular increase of the local von Mises strain for higher global strains ( $\varepsilon_g$  0.8% and 1.2%). The average wavelength of the strain profile is of the order of 444  $\mu\text{m}$  with a corresponding profile amplitude of about 0.75%. The curves for both specimens show a strong local strain increase at the global strain before fracture (specimen 1,  $\varepsilon_g$  1.77% and specimen 2, 1.29%) which originates from strain localization zones that extended into the section just before fracture.

### 3.3.3. Point analysis of local strains

In addition to the evaluation of the evolution of the local strain profiles we compared the local strain evolution in two selected domains with different local von Mises strain developments during testing by performing a point analysis. The point analysis shows the evolution of the von Mises strain at a single point as a function of increasing global strain during testing. For every sample, ten points were defined in domains where the local von Mises

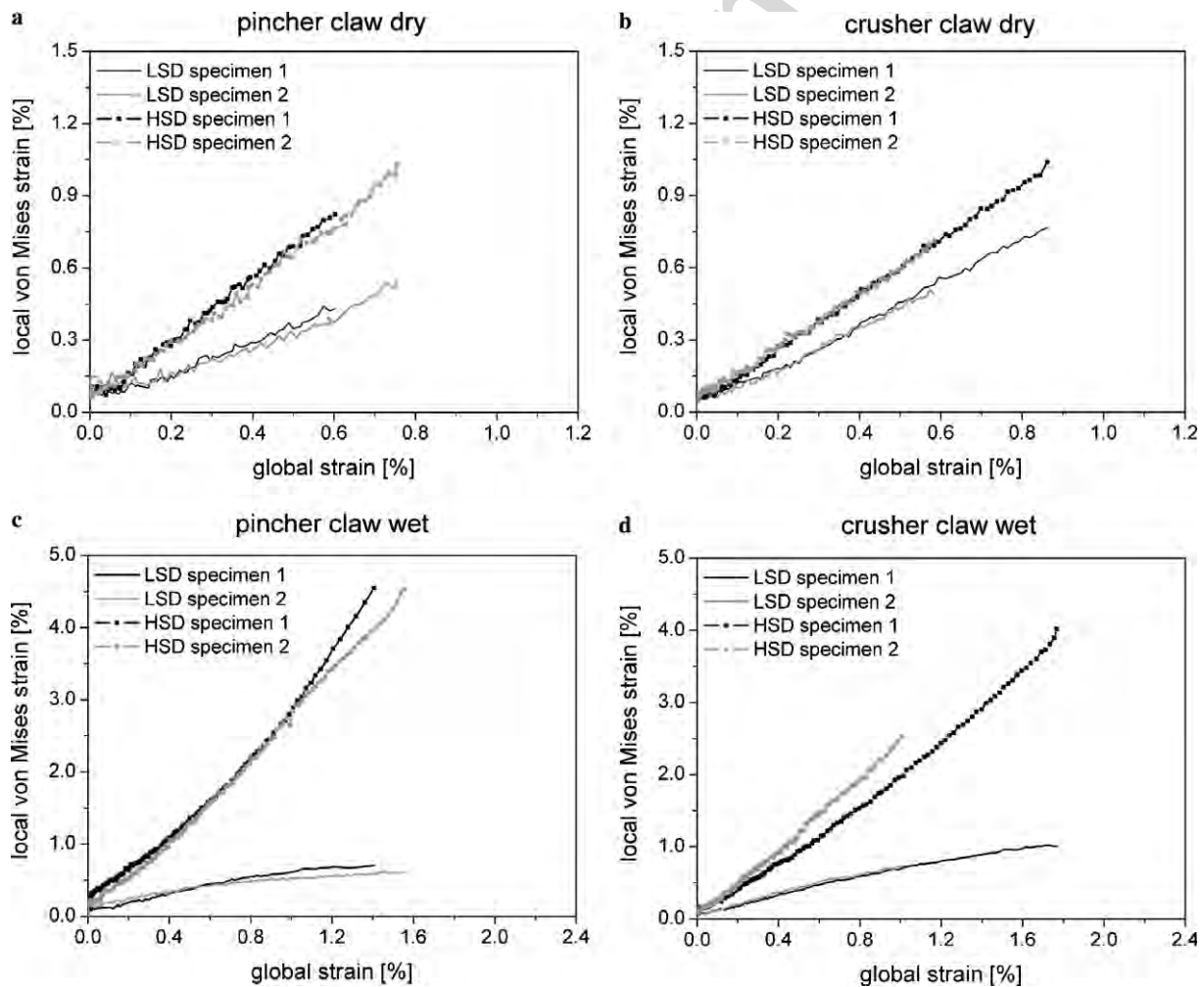


Fig. 14. Point analysis showing the evolution of the local von Mises strain as a function of increasing global strain during tensile testing. For every tested specimen of the dry pincher claw (a), the dry crusher claw (b), the wet pincher claw (c) and the wet crusher claw (d) ten points were defined in domains where the local strain remains low (low strain domains, LSD) and ten points were defined in domains where the local strain increases strongly (high strain domains, HSD). The values of the local strain in every point were averaged and plotted as von Mises strain (%) against the global strain.

Table 3  
Average local strain evolution rates ( $\delta$ ) for the low strain domains (LSD) and the high strain domains (HSD) determined for every set of samples

Sample	Average strain evolution rate $\delta$ for low strain domains (–)	Average strain evolution rate $\delta$ for high strain domains (–)
Pincher claw dry	0.53	1.24
Crusher claw dry	0.81	1.11
Pincher claw wet	0.42	2.79
Crusher claw wet	0.64	2.23

$\delta$  is given as von Mises strain (%) per global strain (%) and is dimensionless.

strain remains low (low strain domains, LSD) and ten points were defined in domains where the local von Mises strain increases strongly (high strain domains, HSD). A strain evolution rate  $\delta$  was defined as the gradient of local von Mises strain  $\varepsilon_M$  over the global strain  $\varepsilon_g$  according to  $\delta = \frac{d\varepsilon_M}{d\varepsilon_g}$ . The values of the strain evolution rate  $\delta$  are given as the slope of curves averaged out of the data from 10 points located in low strain domains and 10 points located in high strain domains on each test specimen (Fig. 14, Table 3).

The point analysis for pincher and crusher claw in dry condition shows that the von Mises strain evolves fairly linearly with increasing global strain but with different evolution rates for low and high strain domains. For the dry pincher claw samples the strain evolution rate  $\delta$  is 0.53 for the low strain domains and 1.24 for the high strain domains (Fig. 14a). The strain evolution rates are quite similar for the dry crusher claw samples with  $\delta$  amounting to 0.81 for the low strain domains and 1.11 for the high strain domains (Fig. 14b).

In the wet pincher and crusher claw the local von Mises strain evolution is also rather linear for both low and high strain domains. Compared with the dry samples the evolution rates are similar in the low strain domains but increase to about the double value for the high strain domains. For the wet pincher claw samples the strain evolution rate  $\delta$  amounts to 0.42 in the low strain domains and 2.79 in the high strain domains (Fig. 14c). The wet crusher claw reaches strain evolution rates of 0.64 for the low strain domains and 2.23 for the high strain domains (Fig. 14d).

#### 4. Discussion

The understanding of the mechanical functions of arthropod exoskeletons, such as movement, joint formation, and the exertion of and protection against external forces, requires a precise determination of the local mechanical properties of the material. In biological composite materials these mechanical properties are determined by three groups of parameters: the internal material composition including its structure on all levels of organization, the physiological state of the sample, and its artificial or preparation state, respectively. The

material composition is determined by the types and quantities of molecules forming the respective material, in this case  $\alpha$ -chitin as scaffold, various structural and functional proteins, calcium carbonate in different crystalline modifications as well as magnesium, phosphate and water. The interactions between the different components determine the structure of the composite material starting from the level of molecular constitution on the nano-scale, the assembly of structural subunits like fibrils and fibers forming a twisted plywood structure on the micrometer and millimeter scale to the formation of functional units of the organism like the chelipeds or other body parts. The structure of the material can be described in terms of a number of internal variables such as its mass density, stacking density of planes, porosity, crystallographic texture of its crystalline constituents, average diameter of the chitin fibers, or particle size of the minerals to name just a few (Raabe et al., 2005a,b,c; Raabe et al., 2006).

Beyond these *internal* structural and composition measures the actual state of a biological material can also be described in terms of a number of essential *physiological* parameters. The physiological state of the organism plays a particularly important role for the material such as for example the actual stage of the molting cycle or the general environmental and living conditions like pH, salt content, temperature, nutrition or diseases (Fabritius and Ziegler, 2003; Ziegler et al., 2005).

A third category affecting the mechanical state of the material under inspection which profoundly differs from the two others is its *artificial* condition which is obtained by sample preparation owing to the *externally* imposed boundary conditions. Parameters belonging to this group are storage conditions, the grade of hydration and effects caused by the natural decomposition of certain components. All these parameters can influence each other and they collectively define the structural state of the material and hence its mechanical properties.

For the experimental examination of the mechanical properties of biomaterials it is crucial to establish a defined state of the test specimens, preferably as close as possible to its original natural state in order to obtain authentic values for the material in its incipient functional state under conditions set by the typical biological environment. In our experiments, we took these aspects into account by performing identical strain experiments on dry and wet claw endocuticle, since it is particularly the water content which is known to strongly influence the properties of biological composites.

A constraint for the quantitative determination of the mechanical properties is the limited number of test specimens which can be obtained from the crusher and the pincher claw of an individual lobster. The application of statistical methods requires an adequate data set whose size depends on the amount of variables. Consequently, the multiple varying physiological parameters which have to be taken into account when testing samples from different lobsters would increase the data set required to obtain

statistically significant results dramatically. Hence, in this study the quantitative values of the mechanical properties are obtained from test specimens of only one lobster. These values may vary to a certain extent for other specimens of *Homarus americanus*. Due to the experimental design, only the mechanical properties of the endocuticle are evaluated in this study. Concerning the mechanical properties of the whole procuticle, both the endocuticle and the exocuticle contribute to its mechanical response. The structural stiffness of the procuticle is the sum of the structural stiffness of the endocuticle and the exocuticle with respect to their cross-sectional fractions. Nano-indentation experiments show that the reduced elastic modulus  $E_{\text{red}}$  which is defined by the ratio of the elastic modulus to Poisson's ratio  $\nu$ ,  $E_{\text{red}} = \frac{E}{1-\nu^2}$ , is about 20% higher in the exocuticle than in the endocuticle (Sachs et al., 2006). Assuming that this ratio is also valid for the structural stiffness, the structural stiffness of the procuticle can be estimated. The exocuticle reaches a constant thickness of around 200  $\mu\text{m}$  in the mineralized parts of the lobster exoskeleton, whereas the thickness of the endocuticle varies strongly. Thus, the structural stiffness of the procuticle is dependent on the thickness of the endocuticle, the thicker the endocuticle, the smaller the influence of the exocuticle.

The global stress–strain behavior of lobster endocuticle reveals a pronounced discrepancy between the wet and the dry specimens (Fig. 7, Table 1). In the dry state the pincher and crusher claw display a linear elastic behavior typical of brittle response. In contrast the wet specimens showed an onset of plastic deformation which begins at a yield strain  $\varepsilon_y$  of 0.5% and extends to a strain to fracture  $\varepsilon_f$  of about 1.8% and 1.7%, respectively. The comparison to the strain to fracture of 0.7% achieved by the dry samples shows the absence of mechanisms allowing deformation and stress reduction in dehydrated endocuticle. In the wet samples, the maximal achieved strain and stress correspond nearly to the strain and stress to fracture, which indicates that significant necking did not occur in the tensile test specimens at the end of deformation. While the absence of necking is typical for brittle materials it is untypical for more ductile materials such as the wet samples in the current case. Similar differences in deformation behavior were observed for untreated cuticle in the dry and the wet state taken from the walking legs of the crab *Scylla serrata* (Hepburn et al., 1975) and the carapace of the prawn *Penaeus mondon* (Joffe et al., 1975).

For the elastic behavior, the resulting structural stiffness  $s_{\text{st}}$  values differ only slightly between the samples taken from the different claws but the difference is more pronounced between the dry and the wet state. The structural stiffness  $s_{\text{st}}$  of the dry samples lies between 5.8 and 7.0 GPa which is higher than in the wet samples with about 4.8 GPa. The difference in structural stiffness between dry (1.1 GPa) and wet state (0.4 GPa) reported for crab and prawn cuticle in literature (Hepburn et al., 1975) is much more pronounced than in lobster claws. The comparably small difference in structural stiffness between dry and

wet endocuticle in the lobster can probably be explained with the relatively high content of minerals in the claws whose elastic properties are less affected by the water content than the organic constituents (Vincent, 2002).

The effect of water acting as a *plastifier* for the probably irreversible deformation behavior becomes apparent by comparing the fracture surfaces of the samples tested in dry and in wet state (Vincent and Wegst, 2004). The crack which caused the failure of the dry test specimens propagated through the twisted plywood structure in two different ways: First, by cleaving of fibers which were oriented more parallel to the fracture surface longitudinally along their junctions or, second, by cutting the fibers which were oriented more perpendicularly to the fracture surface normal to the fiber axis. Due to the rotation in the stacked fiber planes and the fixed fracture plane, the fracture surface subsequently shows an alternation of these two types of fracture modes. The residual overlapping platelets display smooth facets corresponding to a brittle catastrophic failure, since typical features of plastic deformation or gradual delamination effects which impede crack growth are not visible. The cleaved cuticular pores oriented in normal direction which recur on the fracture surfaces probably act as natural defects in the material. Additionally, during the drying process internal stresses can generate microcracks which possibly add up to these naturally present defects. Such an agglomeration of defects and microcracks can lead to a critical crack size resulting in a brittle failure as also known from various ceramic materials (Suresh, 2004). The combination of these effects leave the original microstructure below the fracture surface almost unaltered.

On the other hand, the fracture surfaces of the wet pincher and crusher claw reveal distinct deformation features indicating a different type of fracture mechanism. In these samples the twisted plywood structure appears strongly distorted and split up with its fibrous components aligned in tensile direction. The bundles of fibers which were originally oriented more or less perpendicular to the fracture surface slid and were torn apart which is an indication for delamination inside the twisted plywood layers. Additionally, the junctions between the fibers at the torn ends of the bundles are separated by flexible pore canal tubes which are stabilized by the mainly parallel oriented parts of adjacent twisted plywood layers and thus remain located in their original position. Those pore canal tubes which are torn out of the honeycomb structure protrude out of the fracture plane. The obliquely oriented parts of the honeycomb structure become arranged along the tensile direction during elongation most likely caused by delamination, rotation and deflection, which are indications for microplasticity. Simultaneously, the honeycomb structure is divided into bundles in which the pore canals appear slightly compressed and elongated. The fibers oriented parallel to the fracture surface seem not to be deformed plastically but appear to have delaminated in a similar way as in the dry samples, although probably less pronounced. The described mechanisms indicate the occur-

rence of toughening effects such as crack deflection and bridging of the cracks which both lead to stepwise crack propagation before the actual fracture. This stepwise crack propagation becomes obvious in the strain maps recorded for the wet samples during tensile testing (Fig. 11) in which the appearance of a crack, further crack opening and the crack propagation are indicated by strong strain localizations evolving along the pathway of the crack.

The local strain analysis of the endocuticle can provide information about the correlation between the microstructure, the local mechanical properties and the underlying deformation behavior. The dry samples and the wet samples show pronounced heterogeneous strain patterns with a relatively even distribution of domains with low local strain and domains with elevated local strain. The domains display a similar development during the tensile test, but at a lower global strain level for the dry samples (Fig. 10) compared to the wet samples (Fig. 11). The relatively uniform appearance of the strain patterns is generated by a similar distribution of the low and high local strain domains in both wet and dry samples as shown by the analysis of the strain profiles (Figs. 12 and 13). This distribution is characterized by a specific wavelength which is of the order of 430  $\mu\text{m}$  for the dry samples and 460  $\mu\text{m}$  for the wet samples and describes the initial size of the different local strain domains (see Table 2). The formation of characteristic local strain patterns can be the result of variations and inhomogeneities of the microstructure. Such variations of the microstructure would be for example the cuticular pores, which can act as natural defects in the material as indicated by the analysis of the fracture surfaces. A periodicity in the arrangement of these pores could eventually generate a distinct local strain pattern, but if they play a role in this for the lobster endocuticle remains to be cleared. However, the capability of microstructural features to generate strain patterning in biological materials has been shown for Haversian canals in bone (Kim et al., 2005). Variations of the material composition, mainly the grade of mineralization, might also affect the local deformation behavior. Earlier reports on the events during the beginning of the mineralization of the new cuticle of crabs after the molt show that crystalline calcium carbonate germs nucleate in the outermost cuticle layers which form flat discs and later spherulites that grow radially along the vertical axis of the cuticle (Giraud-Guille and Bouligand, 1995). This radial growth causes neighboring spherulites to fuse, possibly creating boundaries in the areas of contact. Assuming that these boundaries affect the local mechanical properties and the mechanism of mineralization in the lobster cuticle is similar, this could also be a possible hint for the generation of the strain patterning observed in the lobster. However, the average diameter of these spherulites in crab cuticle seems to be about 200  $\mu\text{m}$  whereas the wavelength of the strain patterns in the lobster is in the order of 450  $\mu\text{m}$ . Surface roughness as cause for the strain patterns can be excluded since our samples have a roughness of about 2  $\mu\text{m}$  after the machining process and

the depth of surface defects would have to be much larger in comparison to the sample thickness in order to affect the local mechanical properties. Further investigation is required to explain the origins of the strain patterns.

The evolution of the strain patterns does not differ greatly between pincher and crusher claw, neither in the dry state nor in the wet state (Table 2). However, distinct differences can be observed between the dry (Fig. 12) and the wet samples (Fig. 13). With increasing global strain the von Mises strain profiles of the dry samples retain their overall shapes and are merely shifted towards higher values. For a global strain of 0.6%, their amplitude reaches a value in the order of 0.2% with a lower threshold of about 0.5%. Remarkably, for the double amount of global strain (1.2%) the lower threshold of the wet samples amounts to the only slightly higher value of 0.8% whereas the amplitude is increased about four times to 0.9% compared to the dry samples (see Table 2). The point analysis gives further details about the evolution of the local strain in the low strain domains and the high strain domains. In the low strain domains the strain evolution rate  $\delta$  is in a similar range for both the dry (Fig. 14a and b) and the wet samples (Fig. 14c and d). In the high strain domains of the dry samples  $\delta$  is only slightly higher than in the low strain domains, but becomes more than twice as high in the wet samples (see Table 3). Noteworthy is the linear relationship between the global strain and the local strain which was also observed in cortical bone (Kim et al., 2005). A possible reason for the pronounced difference between the development of the low and high strain domains in the dry and the wet samples is the primarily elastic response and the limited plasticity in the dry state, obviously constricting the formation of domains which carry out the plastic deformation in the wet samples after reaching the yield strain.

Before the brittle failure of the dry samples, strain localization zones do not necessarily appear early in the areas of fracture (Fig. 10). Strain accumulations leading to a catastrophic fracture obviously formed in less than 1 s, the time interval between the strain map recorded immediately before fracture (Fig. 10b–d) and the next image recorded by the experimental setup (not shown). The strain patterns of the wet samples include domains in which the strain continues to increase while the strain evolution attenuates in the domains of lower strain. Before failure some of these domains form strain localizations in which the crack initiation takes place. The incipient crack evolves from the edge and grows stepwise following the expanding strain localization zone until complete fracture occurs (Fig. 11). This fracture behavior is caused by the existence of microplasticity and delamination effects in the twisted plywood structure which precede the actual failure event.

Comparable complex microstructures and micromechanical behavior are observable in commercially produced advanced polymer composites. Their excellent mechanical properties arise from the combination of components with the desired mechanical properties. Smart design strategies enable tailored materials for various applications. For

instance, polymers reinforced with short glass fibers show similar well defined strain patterns depending on the distribution and orientation of the fibers (Godara and Raabe, 2006). The interaction of the different components causes heterogeneous strain patterns including zones of strain localizations, much as observed in our natural material.

## 5. Conclusions

In this study, we examined the deformation behavior of the endocuticle of the lobster *Homarus americanus* in dry and wet state. In order to conduct both, global and local strain analysis with high lateral resolution we applied a novel experimental approach for the mapping of the displacement gradient and strain fields during tensile testing, namely, digital image correlation. The tensile tests revealed two main factors influencing the deformation and fracture behavior. The first one is the moisture of the samples. The dry samples failed catastrophically in a brittle manner in the linear elastic region. The fracture took place perpendicular to the tensile direction. On the other hand, the natural wet samples showed a pronounced plastic region and stepwise crack propagation before fracture. This behavior can be caused by the existence of microplasticity and toughening effects like crack deflection and crack bridging due to delamination effects in the twisted plywood structure.

The local strain patterns were found to be heterogeneous in the dry state and in the wet state. The wavelength of the strain patterns (peak-to-peak spacing) was of the order of 430  $\mu\text{m}$  for the dry sample and 460  $\mu\text{m}$  for the wet samples.

In both the dry and the wet state the development of domains with low local strain and domains with high local strain could be observed. This phenomenon occurred, however, at much larger global strains in the wet samples. Also, the increase of global strain leads to a uniform increase in local strain in the low and high strain domains of the dry samples whereas in the wet samples the high strain domains reach much higher strains compared to the low strain domains. This micromechanical difference between the dry and the wet state indicates that the presence of moisture enhances the ability for plastic deformation in certain domains of the samples during mechanical loading.

We discussed several reasons which are conceivable to entail such strain heterogeneity upon loading. These include local differences in the grade of mineralization which would lead to a modification in the local mechanical properties and the influence of the distribution of natural defects like cuticular pores in the material.

## References

- Andersen, S.O., 1979. Biochemistry of insect cuticle. *Ann. Rev. Entomol.* 24, 29–61.
- Andersen, S.O., 1999. Exoskeletal proteins from the crab *Cancer pagurus*. *Comp. Biochem. Physiol. A* 123, 203–211.
- Ashby, M.F., Wegst, U.G.K., 2004. The mechanical efficiency of natural materials. *Philos. Mag.* 84, 2167–2181.
- Becker, A., Ziegler, A., Epple, M., 2005. The mineral phase in the cuticles of two species of Crustacea consists of magnesium calcite, amorphous calcium carbonate, and amorphous calcium phosphate. *Dalton Trans.* 2005, 1814–1820.
- Blackwell, J., Weih, M.-A., 1980. Structure of chitin-protein complexes: ovipositor of the ichneumon fly, *Megagrhyssa*. *J. Mol. Biol.* 137, 49–60.
- Bouligand, Y., 1970. Aspects ultrastructuraux de la calcification chez les Crabes, in: 7e Congrès int. Microsc. Électr., Grenoble, France, t. 3, 105–106.
- Carpenter, K.E., 2002 (Ed.). The living marine resources of the Western Central Atlantic Volume 1: Introduction, molluscs, crustaceans, hagfishes, sharks, batoid fishes, and chimaeras. *FAO Species Identification Guide for Fishery Purposes*, American Society of Ichthyologists and Herpetologists Special Publication No. 5, Rome, FAO, 1–600.
- Compère, Ph., 1995. Fine structure and morphogenesis of the sclerite epicuticle in the Atlantic shore crab, *Carcinus maenas*. *Tissue Cell* 27, 525–538.
- Compère, Ph., Morgan, J.A., Winters, C., Goffinet, G., 1992. X-ray microanalytical and cytochemical study of the mineralization process in the shore crab cuticle. *Micron Microsc. Acta* 23, 355–356.
- Currey, J.D., 1967. The failure of exoskeletons and endoskeletons. *J. Morphol.* 123, 1–16.
- Currey, J.D., 1996. Biocomposites: micromechanics of biological hard tissue. *Curr. Opin. Solid State Mater. Sci.* 1, 440–445.
- Dillaman, R.M., Hequembourg, S., Gay, M., 2005. Early pattern of calcification in the dorsal carapace of the blue crab, *Callinectes sapidus*. *J. Morphol.* 263, 356–374.
- Elices, M., 2000. *Structural Biological Materials: Design and Structure–Property Relationships*. Pergamon, New York.
- Fabritius, H., Ziegler, A., 2003. Analysis of  $\text{CaCO}_3$  deposit formation and degradation during the molt cycle of the terrestrial isopod *Porcellio scaber* (Crustacea, Isopoda). *J. Struct. Biol.* 142, 281–291.
- Gao, H., Ji, B., Jaeger, I.L., Arzt, E., Fratzl, P., 2003. Materials Become Insensitive to Flaws at Nanoscale: Lessons from Nature. *Proc. Natl. Acad. Sci. USA* 100, 5597.
- Giraud-Guille, M.-M., 1984. Fine structure of the chitin-protein system in the crab cuticle. *Tissue Cell* 16, 75–92.
- Giraud-Guille, M.-M., 1990. Chitin crystals in arthropod cuticles revealed by diffraction contrast transmission electron microscopy. *J. Struct. Biol.* 103, 232–240.
- Giraud-Guille, M.-M., 1998. Plywood structures in nature. *Curr. Opin. Solid State Mater. Sci.* 3, 221–228.
- Giraud-Guille, M.-M., Bouligand, Y., 1995. Crystal growth in a chitin matrix: the study of calcite development in the crab cuticle. In: Karnicki, Z.S. (Ed.), *Chitin World*. *Wirtschaftsverlag NW*, Bremerhaven, pp. 136–144.
- Godara, A., Raabe, D., 2006. Micromechanical behavior of thermoplastic matrix composites by digital image correlation. *Proc. of the 27th Int. SAMPE Europe Conference 2006*, 121–126.
- GOM, Handbook for the Aramis system, Gesellschaft fuer Optische Meßtechnik mbh, Version September 2000, Braunschweig, Germany.
- Hadley, N.F., 1986. The arthropod cuticle. *Sci. Am.* 255, 98–106.
- Hepburn, H.R., Joffe, I., Green, N., Nelson, K.J., 1975. Mechanical properties of a crab shell. *Comp. Biochem. Physiol.* 50A, 551–554.
- Horst, M.N., Freeman, J.A. (Eds.), 1993. *The Crustacean Integument: Morphology and Biochemistry*. CRC Press, Ann Arbor, Michigan, USA.
- Joffe, I., Hepburn, H.R., Nelson, K.J., Green, N., 1975. Mechanical properties of a crustacean exoskeleton. *Comp. Biochem. Physiol.* 50A, 545–549.
- Kim, D.J., Brunski, J.B., Nicoletta, D.P., 2005. Microstrain fields for cortical bone in uniaxial tension: optical analysis method. *Proc. IMechE*, vol. 219 Part H: *J. Eng. Med.*, 119–128.

- Lowenstam, H.A., 1981. Minerals formed in organisms. *Science* 211, 1126–1131.
- Lowenstam, H.A., Weiner, S., 1989. *On Biomineralization*. Oxford University Press, New York.
- Mann, S., 1995. Biomineralization and biomimetic materials. *Chemistry J. Mater. Chem.* 5, 935.
- Mann, S., Webb, J., Williams, R.J.P., 1989. *On Biomineralization*. VCH Press, New York.
- Manoli, F., Koutsopoulos, S., Dalas, E., 1997. Crystallization of calcite on chitin. *J. Cryst. Growth* 182, 116.
- Melnick, C.A., Chen, S., Mecholsky, J.J., 1996. Hardness and toughness of exoskeleton material in the stone crab *Menippe mercenaria*. *J. Mater. Res.* 11, 2903–2907.
- Neville, A.C. (Ed.), 1993. *Biology of Fibrous Composites*. Cambridge University Press.
- Raabe, D., Sachtleber, M., Zhao, Z., Roters, F., Zaefferer, S., 2001. Micromechanical and macromechanical effects in grain scale polycrystal plasticity experimentation and simulation. *Acta Mater.* 49, 3433–3441.
- Raabe, D., Sachtleber, M., Weiland, H., Scheele, G., Zhao, Z., 2003. Grain-scale micromechanics of polycrystal surfaces during plastic straining. *Acta Mater.* 51, 1539–1560.
- Raabe, D., Romano, P., Sachs, C., Al-Sawalmih, A., Brokmeier, H.-G., Yi, S.-B., Servos, G., Hartwig, H.G., 2005a. Discovery of a honeycomb structure in the twisted plywood patterns of fibrous biological nanocomposite tissue. *J. Cryst. Growth* 283, 1–7.
- Raabe, D., Sachs, C., Romano, P., 2005b. The crustacean exoskeleton as an example of a structurally and mechanically graded biological nanocomposite material. *Acta Mater.* 53, 4281–4292.
- Raabe, D., Al-Sawalmih, A., Romano, P., Sachs, C., Brokmeier, H.-G., Yi, S.-B., Servos, G., Hartwig, H.G., 2005c. Structure and crystallographic texture of arthropod bio-composites. *Mater. Sci. Forum* 495–497, 1665–1674.
- Raabe, D., Romano, P., Sachs, C., Fabritius, H., Al-Sawalmih, A., Yi, S.-B., Servos, G., Hartwig, H.G., 2006. Microstructure and crystallographic texture of the chitin-protein network in the biological composite material of the exoskeleton of the lobster *Homarus americanus*. *Mater. Sci. Eng. A* 421, 143–153.
- Raz, S., Testiniere, O., Hecker, A., Weiner, S., Luguët, G., 2002. Stable amorphous calcium carbonate is the main component of the calcium storage structures of the crustacean, *Orchestria cavimana*. *Biol. Bull.* 203, 269–274.
- Roer, R.D., Dillaman, R.M., 1984. The structure and calcification of the crustacean cuticle. *Am. Zool.* 24, 893–909.
- Sachs, C., Fabritius, H., Raabe, D., 2006. Hardness and elastic properties of dehydrated cuticle from the lobster *Homarus americanus* obtained by nanoindentation. *J. Mater. Sci.*, in press.
- Sachtleber, M., Zhao, Z., Raabe, D., 2002. Experimental investigation of plastic grain interaction. *Mater. Sci. Eng. A* 336, 81–87.
- Shen, Z., Jacobs-Lorena, M., 1999. Evolution of chitin-binding proteins in invertebrates. *J. Mol. Evol.* 48, 341–347.
- Suresh, S., 2004. *Fatigue of Materials*, second ed. Cambridge University Press, Cambridge.
- Travis, D.F., 1963. Structural features of mineralization from tissue to macromolecular levels of organization in the Decapoda Crustacea. *Ann. N. Y. Acad. Sci.* 109, 177–245.
- Vernberg, F.J., Vernberg, W.B. (Eds.), 1983. *The Biology of Crustacean*. Academic Press, New York, USA.
- Vincent, J.F.V. (Ed.), 1990. *Structural Biomaterials*. Princeton University Press, USA.
- Vincent, J.F.V., 2002. Arthropod cuticle: a natural composite shell system. *Composites A* 33, 1311–1315.
- Vincent, J.F.V., Currey, J.D. (Eds.), 1980. *Mechanical Properties of Biological Materials*. Society for Experimental Biology, Cambridge, UK.
- Vincent, J.F.V., Wegst, U.G.K., 2004. Design and mechanical properties of insect cuticle. *Arthropod Struct. Dev.* 33, 187–199.
- Weiner, S., Addadi, L., 1997. Design strategies in mineralized biological materials. *J. Mater. Chem.* 7, 689–702.
- Weiner, S., Wagner, H.D., 1998. The material bone: structure-mechanical function relations. *Annu. Rev. Mater. Sci.* 28, 271.
- Zaefferer, S., Kuo, J.-C., Zhao, Z., Winning, M., Raabe, D., 2003. On the influence of the grain boundary misorientation on the plastic deformation of aluminum bicrystals. *Acta Mater.* 51, 4719–4735.
- Ziegler, A., Fabritius, H., Hagedorn, M., 2005. Microscopical and functional aspects of calcium-transport and deposition in terrestrial isopods. *Micron* 36, 137–153.